Filter design and color correction for the *X*-cube prism 3CCD camera

Suhao Chen,[1,2] **Bo Lü,**[1,*] **Xiaotian Wu,**[1] **Weiqi Liu,**[1] **and Qipeng Lü**[3]

[1]*Changchun Institute of Optics, Fine Mechanics and Physics, Chinese Academy of Sciences, Changchun, Jilin 130033, China*
[2]*University of Chinese Academy of Sciences, Beijing 100039, China*
[3]*Key Laboratory of Chemical Lasers, Dalian Institute of Chemical Physics, Chinese Academy of Sciences, Dalian 116023, China*
Corresponding author: jllvbo@163.com

For the *X*-cube prism three-charge-coupled-device (3CCD) camera, the spectra of the designed dichroic films in the *X*-cube prism shift with changes in the angle of incident light, producing non-uniformity of color on the image plane. We considered the influence of the incident angle on color performance in filter design and directly optimized the thin film to improve color consistency. An optical model was constructed to calculate the distribution of camera spectral sensitivity and independently correct the non-uniform color on the image plane. Results showed that the optimization and correction methods could significantly improve the color performance of the *X*-cube prism 3CCD camera.   © 2023 Optica Publishing Group

1. INTRODUCTION

In digital color imaging, the main goals of designing color imaging devices are accurately recording and reproducing the color of an object. According to trichromatic theory, any color can be matched using the three colors of light, which are called the three primary colors, and the number of matching colors is called the tristimulus value [1]. The Commission Internationale de l'Eclairage (CIE) used the three primary colors to match monochromatic lights through psychological experiments and obtained the color matching functions (CMFs), which define the standard color space and provide a consistent color specification standard [2,3].

To record colors accurately, camera spectral sensitivity (CSS) needs to satisfy the Luther condition, which states that perfect color reproduction requires the CSS to be a linear combination of CMFs. However, practically, because of filter design limitations, processing errors, and other factors, the Luther condition is difficult to satisfy completely, and thus, there is a need for optical filter design and color correction to improve the color performance of the camera. The Luther condition clearly indicates that a camera produces better color performance when its spectral sensitivities are closer to the CMFs; therefore, we required quality metrics to evaluate how far a CSS could deviate from a linear combination of the CMFs [4].

The quality factor (*Q*-factor), which was first introduced by Neugebauer [5], can be used to evaluate the closeness of a single CSS with the CMF; however, when multi-channel systems are evaluated, the *Q*-factor may become unreliable. Vora and Trussell [6,7] extended the *Q*-factor as a measure of goodness (MOG), making it possible to use it to evaluate the color performance of multichannel camera spectra. Vora's MOG was designed to minimize the mean squared error (MSE) in the CIE XYZ space. However, since this color space was perceptually non-uniform, the color error in the CIE XYZ space was not directly related to the perceptual color error.

A better metric that would minimize color errors in perceptual uniform color spaces such as CIELAB is needed. Vrhel and Trussell [8] used a nonlinear numerical optimization method to optimize the required filter by minimizing the average and maximum color errors in CIELAB space. However, because of the nonlinear properties of uniform color space, calculating the color error measure in CIELAB space would greatly increase the required number of calculations. Wolski *et al.* [9], Sharma and Trussell [10], and Quan *et al.* [11] proposed a method wherein the transformation from CIE XYZ space to CIELAB space was linearized to estimate the MSE in CIELAB space; the linearization reduced the computational complexity while preserving the colorimetric properties of uniform color space, and also taking into account the effects of system noise and various lighting conditions.

All the aforementioned optimization methods have a common feature: during the optimization process, a 3×3 transform matrix was used to perform mapping from the red-green-blue (RGB) space of the camera to CIE XYZ space. This method is called linear color correction (LCC) in the image-processing pipeline. The most significant advantage of the LCC method is its linearity, making it the easiest correction method to calculate; also, the correction results will not be affected by changes in light intensity [12].

Although LCC is currently the most widely used correction method, many studies have proposed advanced color correction methods to obtain smaller color errors, including polynomial color correction (PCC) [13,14], root-PCC (RPCC) [12], look-up tables (LUTs) [15], hue plane preserving color correction (HPPCC) [16], and neural networks [17]. Compared with the LCC method, these methods can significantly improve the color performance of a camera when the CSS cannot meet the Luther condition. Correspondingly, when we optimize the filter, if we still use the 3×3 transformation matrix to calculate the merit function, the actual color performance of the camera may not be truly reflected.

Additionally, when designing the color filter of the camera, under the existing method, the ideal CSS is usually first designed and then the thin film design is carried out. This method has relatively good performance when used for designing Bayer filters because the results of the thin film design usually do not deviate significantly from the ideal value. However, when designing the filter of the X-cube prism 3CCD camera, CSS is realized by the light splitting of the two dichroic films in the X-cube prism, and the light has a large incident angle on the film. Owing to the properties of dielectric film, this results in a large spectral shift of the film when the angle of incidence changes [18]. Since the imaging broad beam of each field of view (FOV) on the image plane has different incident angle distributions on the film, this may cause serious color non-uniformity in the image. In this case, if we still optimize the ideal CSS first and then design the thin film, it will be difficult to evaluate the non-uniform color error caused by the change of incident angle during optimization, and the designed thin film under a large incident angle may result in a large deviation from the ideal curve.

To solve this problem, we needed a new method to evaluate the effect of the spectral shift caused by the change of the incident angle on the camera's color performance and use this new merit function to design the filter. We also needed to analyze the distribution of CSS on the image plane and independently perform color correction to reduce the color non-uniformity. We analyzed the incident angle distribution of the imaging light on the X-cube prism film through optical modeling and used the incident angle distribution function combined with the performance function of the film to construct a merit function of system color error—which considered the influence of the incident angle—to directly optimize the film in the thin film design software. After obtaining the optimal thin film, FOV sampling and interpolation methods were used to calculate the CSS and correction matrix of the full FOV to achieve independent color correction of the entire image plane.

2. BACKGROUND

A. Imaging Model

The vector imaging model represents the baseline for CSS optimization. In this model, the color of an object can be defined using tristimulus values, and its matrix-vector equation is expressed as follows:

$$t = A^T L r, \qquad (1)$$

where t is a 3×1 vector representing the tristimulus value for CIE XYZ color space ($t = [X, Y, Z]^T$); matrix A is an $N \times 3$ matrix, where the columns of matrix A are CMFs $\bar{x}(\lambda)$, $\bar{y}(\lambda)$, and $\bar{z}(\lambda)$ [19]; N represents the number of spectral samples when sampling at 10 nm intervals over the range of $380 - 780$ nm—$N = 41$; r is an $N \times 1$ vector, which represents the sample reflectance; and L is an $N \times N$ diagonal matrix, wherein the illuminant spectrum lies along the main diagonal.

The matrix-vector equation for the three-channel response value of the camera is like that in Eq. (1):

$$t_c = C^T L r, \qquad (2)$$

where t_c is a 3×1 vector representing the raw camera response ($t_c = [R, G, B]^T$); and $C = [S_R, S_G, S_B]$ is an $N \times 3$ matrix representing the spectral sensitivity of the three RGB channels.

B. Color Correction

To reproduce color information more accurately, it is necessary to perform color correction on the camera. Usually, we map the device-dependent camera RGB space to the device-independent CIE XYZ color space as follows:

$$\hat{t} = \mathcal{F}(t_c), \qquad (3)$$

where $\mathcal{F}(\cdot)$ represents the function of the mapping method, and $\hat{t}$ is the tristimulus value estimated from the raw camera response t_c, which can also be regarded as the corrected tristimulus value. The simplest and most used form of Eq. (3) uses LCC:

$$\hat{t} = M t_c, \qquad (4)$$

where M is a 3×3 transform matrix. In this method, our goal was to obtain matrix M such that the color error between the estimated color and actual color of the sample would be as small as possible. In CIE XYZ space or CIELAB space, the color error can be defined as the Euclidean distance between two points in the corresponding color space [1], and the mean square color error of all the samples can be expressed as

$$\Delta E^2 = E\left\{\| t - \hat{t} \|_2^2\right\}, \qquad (5)$$

where $\|\cdot\|_2^2$ represents the square of l_2-norm, and $E\{\cdot\}$ represents the expectation over the ensemble of samples.

To minimize ΔE^2, the following equation needs to be solved:

$$\underset{M}{\mathrm{argmin}}\, E\{\| t - M t_c \|_2^2\}. \qquad (6)$$

Equation (6) can be solved by performing least-squares regression [20]:

$$M_{\mathrm{opt}} = T T_C^T (T_C T_C^T)^{-1}, \qquad (7)$$

where M_{opt} is the optimal transformation matrix, and T and T_c are $3 \times K$ matrices representing the tristimulus value and camera response for K samples, respectively. The correction matrix M_{opt} obtained using this method could minimize the mean-squared color error of the sample.

Although the LCC method is simple and practical, it produces a larger residual color error when compared with other advanced correction methods. In this study, we selected RPCC as the correction method because it is one of the most effective

color correction methods available, and it works effectively in response to exposure changes like the LCC method does [12,16]. Using the RPCC method, ρ_i can be obtained by extending the camera RGB vector t_c, adding high-order terms, and adding kth roots to each term of the polynomial:

$$\bar{\rho}_3 = [R, G, B]^T$$

$$\bar{\rho}_6 = \left[R, G, B, \sqrt{RG}, \sqrt{RB}, \sqrt{GB}\right]^T$$

$$\bar{\rho}_{13} = \left[R, G, B, \sqrt{RG}, \sqrt{RB}, \sqrt{GB}, \sqrt[3]{RG^2}, \sqrt[3]{RB^2}, \sqrt[3]{GB^2}, \sqrt[3]{R^2G},\right.$$

$$\left.\sqrt[3]{R^2B}, \sqrt[3]{G^2B}, \sqrt[3]{RGB}\right]^T. \tag{8}$$

Using RPCC, Eq. (3) can be written as

$$\hat{t} = M_{3 \times i} \bar{\rho}_i. \tag{9}$$

The $3 \times i$ correction matrix $M_{3 \times i}$ can also be calculated using the method of least squares, and the $\hat{t}$ corrected by RPCC can be obtained.

C. Perceptual Color Error

To evaluate color error in perceptual uniform color space, we converted the color space from CIE XYZ to CIELAB space via the conversion function $\mathcal{F}_{Lab}$:

$$\mathcal{F}_{Lab}(t) = \begin{bmatrix} 116 f\left(\frac{t_2}{w_2}\right) - 16 \\ 500\left(f\left(\frac{t_1}{w_1}\right) - f\left(\frac{t_2}{w_2}\right)\right) \\ 200\left(f\left(\frac{t_2}{w_2}\right) - f\left(\frac{t_3}{w_3}\right)\right) \end{bmatrix}, \tag{10}$$

where $f(x) = \begin{cases} x^{\frac{1}{3}} & x > 0.008856 \\ 7.787x + \frac{16}{116} & x \leq 0.008856 \end{cases}$, and $t = [t_1, t_2, t_3]^T$ and $w = [w_1, w_2, w_3]^T$ denote the CIE XYZ tristimulus values for the sample and white point, respectively.

For a given sample and light source, we can calculate the color error in uniform color space corresponding to the CSS as

$$\Delta E_{ab}^* = E \left\{ ||\mathcal{F}_{Lab}(t) - \mathcal{F}_{Lab}(M_{3 \times i} \bar{\rho}_i)||_2 \right\}. \tag{11}$$

Compared with the color error ΔE in CIE XYZ space, the color error ΔE_{ab}^* in CIELAB space showed greater consistency with the color error perceived by the human eye and could be used as a merit function to optimize the CSS.

C. Optical System Configuration for X-Cube Prism 3CCD Camera

The research in the present study is based on the working of an X-cube prism 3CCD camera. The 3CCD camera comprises a lens, X-cube prism, and three CCD sensors. The general structure of the camera is shown in Fig. 1.

The object light was collected via an imaging lens and entered the prism. This light was then divided into three RGB bands (transmission G, and reflection R, B) by the two dichroic films: blue reflective coating (BRC) and red reflective coating (RRC)
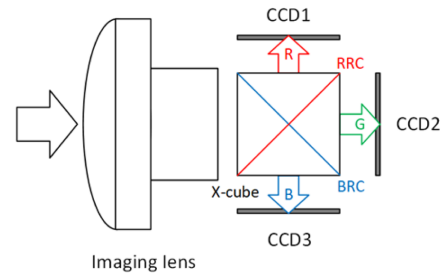

Fig. 1. Optical system for X-cube 3CDD camera.

within the X-cube prism, which were then received by the three-channel detector and finally merged into a color image using image processing methods.

In the X-cube prism 3CCD camera, only $C = [S_R, S_G, S_B]$, in its vector imaging model, differed from that of ordinary cameras. The RGB three-channel spectral sensitivity of the X-cube prism 3CCD camera was mainly dependent on the spectral characteristics of the two dichroic films, BRC and RRC, which were plated on the cemented surface of the X-cube prism. Usually, these two films had a common high-transmittance area within the green band (near 550 nm), where the BRC reflected blue light and the RRC reflected red light. The combination of these two films can divide the visible light into three RGB bands in three directions. The CSS of the X-cube prism 3CCD camera can be represented as

$$S_R = S_{BRC} \times (1 - S_{RRC}) \times S_{IR} \times D_{lens} \times D_{ccd},$$

$$S_G = S_{RRC} \times S_{BRC} \times S_{IR} \times D_{lens} \times D_{ccd},$$

$$S_B = S_{RRC} \times (1 - S_{BRC}) \times S_{IR} \times D_{lens} \times D_{ccd}, \tag{12}$$

where S_{BRC} and S_{RRC} are the transmission spectra of the dichroic film—since the absorption of the dielectric film can be ignored, its reflection spectra can be written as $1 - S_{BRC}$ and $1 - S_{RRC}$, respectively; S_{IR} is the transmittance of the infrared (IR) cutoff filter; and D_{lens} and D_{ccd} represent the transmittance of the lens and response of the detector, respectively.

D. Spectrum Shift Caused by the Change in Incident Angle

However, the optical properties of dichroic filters vary with both the input polarization and angle of incidence; thus, Eq. (12) cannot describe CSS over the entire FOV. In this study, the incident angle distribution on the film surface corresponding to each FOV was completely determined by the front lens group. By optically modeling the optical path of the entire camera, which included the lens, X-cube prism, and dichroic film, the angle of incidence of the chief rays for each FOV on the dichroic film could be calculated to be within the 41°–49° range, and the angle of incidence for the marginal rays was in the 34°–56° range, as shown in Fig. 2(a). At such a large angle of incidence, the film showed a large separation of the transmittance and reflectance spectra for s-polarized and p-polarized light. In contrast, the incident angle on the IR cutoff film was less than 10°, and its spectral shift was very small; therefore, its influence on the color performance of the camera could be ignored in this study.
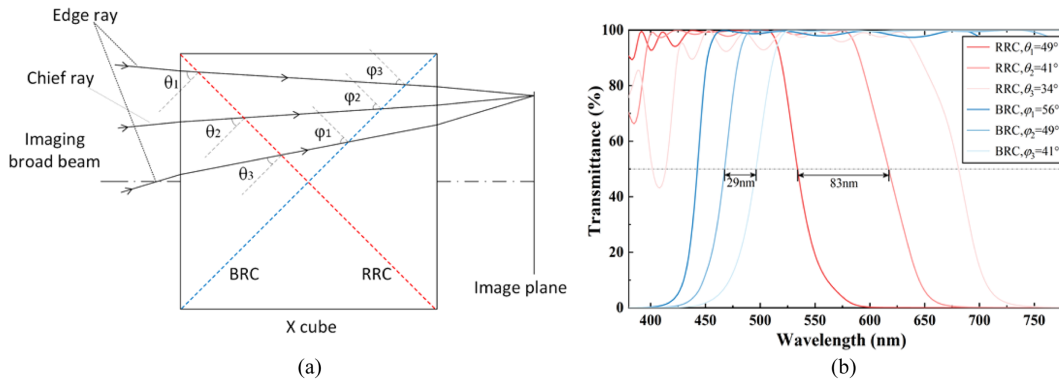
(a)

(b)

Fig. 2.   (a) Angle of incidence in X-cube prism. (b) Spectral shifts of BRC and RRC.

Even if a polarized light design was used, the transmittance spectra of the dichroic films would still show a large deviation with any change in the angle of incidence. Figure 2(b) shows the spectra for s-polarized light incident at $34°$–$56°$ on the originally designed BRC and RRC. The figure shows that at 50% transmittance, the wavelength difference at $41°$–$49°$ incidence reached 83 and 29 nm for RRC and BRC, respectively. This large spectral shift resulted in different spectral sensitivities that corresponded to pixels at different positions on the image plane. In this case, if Eq. (12) was used to optimize the CSS, the influence of the incident angle was ignored, and color correction was performed uniformly on the entire image plane, severely nonuniform colorimetry may occur. Even if we performed color correction independently on the pixels at each position of the image plane, a spectral shift that is too large may make it difficult to correct the color error at the edge of the FOV. Therefore, we needed to analyze the spectral shift of the camera caused by the change in the incident angle and eliminate its influence through film optimization and independent color correction.

We selected a pixel point on the image plane, and its normalized coordinates were (x, y), assuming that the incident angle distribution of the imaging broad beam on the two dichroic films was $P_{RRC}(x, y, \theta)$ and $P_{BRC}(x, y, \theta)$, which represents the proportion of light with different incident angles in the beam corresponding to the image point at (x, y) position, where θ is the incident angle of light on the film, and the transmittance spectra of the two films at the incident angle θ are $F_{RRC}(\theta)$ and $F_{BRC}(\theta)$. Taking RRC for example, the dichroic film transmittance spectrum $S_{RRC}(x, y)$ of the broad beam corresponding to position (x, y) on the image plane can be calculated from the incident angle distribution P and the film spectrum F:

$$S_{RRC}(x, y) = \int F_{RRC}(\theta) P_{RRC}(x, y, \theta) d\theta. \tag{13}$$

The incident angle distribution function P_{RRC} can be calculated by ray tracing, and the film spectrum F_{RRC} can be calculated using the thin film parameters. We used the summation method to simplify the calculation, and took the range of $34°$–$56°$ and interval of $1°$ for the incident angle θ; then Eq. (13) could be written as

$$S_{RRC}(x, y) \cong \sum_{\theta} F_{RRC}(\theta) P_{RRC}(x, y, \theta). \tag{14}$$

For P_{RRC}, we set a group of uniformly distributed parallel ray grids on the image side of the lens according to (x, y), obtained the incident angle of each imaging ray on the dichroic film, and then counted the number of rays N_{RRC} according to the interval of $1°$. Thus, we can get P_{RRC}:

$$P_{RRC}(x, y, \theta) = \frac{N_{RRC}(x, y, \theta)}{\sum_{\theta} N_{RRC}(x, y, \theta)}. \tag{15}$$

After considering the incident angle, the CSS matrix C can be rewritten as matrix $C(x, y) = [S_R(x, y), S_G(x, y), S_B(x, y)]$ related to the image plane position:

$$S_R(x, y) = S_{BRC}(x, y) \times [1 - S_{RRC}(x, y)] \times S_{IR} \times D_{lens} \times D_{ccd},$$

$$S_G(x, y) = S_{RRC}(x, y) \times S_{BRC}(x, y) \times S_{IR} \times D_{lens} \times D_{ccd},$$

$$S_B(x, y) = S_{RRC}(x, y) \times [1 - S_{BRC}(x, y)] \times S_{IR} \times D_{lens} \times D_{ccd}. \tag{16}$$

Similarly, the camera RGB response can be written as

$$t_c(x, y) = C(x, y)^T L r. \tag{17}$$

From Eq. (17), the merit function in Eq. (11), which does not consider the incident angle, can be changed to the merit function $\Delta E_{ab}^*(x, y)$, which considers the influence of the incident angle associated with the image plane position in the X-cube prism 3CCD camera. The color performance of all pixels in the image plane can be comprehensively considered by selecting several sampling points.

3. FILTER OPTIMIZATION METHOD

A. Optimization without Consideration of Incident Angle

If Eq. (17) is to be used to consider the effect of the incident angle when optimizing the film, the distribution function $P_{RRC}(x, y, \theta)$ and spectral properties of the film $F_{RRC}(\theta)$ need to be obtained first. Since we did not have an initial thin film, it is difficult to consider the angle of incidence and optimize the thin film at the beginning. Therefore, we ignored the influence of the incident angle in the first step, used the parameterized method to optimize the film spectrum curve, and then designed the thin film from the spectrum curve. The obtained film could

be used to calculate the spectral characteristic $F_{RRC}(\theta)$, from which an optimization method wherein the angle of incidence was considered could be constructed.

According to Eq. (12), when the lens and detector are determined, the optimization problem of the camera RGB spectrum becomes the optimization problem of the three film spectra of S_{RRC}, S_{BRC}, and S_{IR}. Since the transmittance of the lens and spectral response of the detector were very low below 400 nm, no ultraviolet cutoff was required. The BRC and RRC could be designed as bandpass dichroic filters that transmitted red and green, and reflected blue, and transmitted blue and green, and reflected red, respectively.

To ensure the processability of the film before optimization, we needed to parameterize the filter of the X-cube prism, which helped to reduce the number of calculations required during the optimization process. We used a combination of multiple Gaussian functions of the form $a \cdot \exp(-(\lambda - \mu)^2/\sigma^2)$ to fit the BRC, RRC, and IR-cut transmittance curves. These three filters were all bandpass types, which meant that we could use half a Gaussian curve (divided into two at the vertex) for fitting.

We constructed the synthesized S_R and S_B channel spectral sensitivity functions with reference to the $\bar{x}(\lambda)$ and $\bar{z}(\lambda)$ values of the CMFs; set $S_G = 1 - (S_R + S_B)$ in the working band; deduced the S_{BRC}, S_{RRC}, and S_{IR} transmittance spectra from the RGB three-channel response; and fitted the filter spectrum with Gaussian functions as our starting point for optimization.

After a fitting test, we used three Gaussian functions to fit each filter, which gave the optimized input parameter as a 3×9 matrix, representing nine Gaussian parameters (three groups of a, μ, and σ) for each of the three films. The input Gaussian functions were combined and cropped, and then multiplied by the lens transmittance spectrum and the spectral response of the detector to obtain the $N \times 3$ RGB three-channel spectral sensitivity matrix C and calculate the merit function.

Since many of the metrics proposed in existing literature have simple calculation methods, they provided the advantage of offering a higher calculation speed than that provided from directly using ΔE_{ab}^* as the merit function [7]. In this study, the MOG proposed by Vora and Trussell was used as the first merit function of optimization:

$$\nu = \frac{\text{Trace}\{O^T U U^T O\}}{\text{Trace}\{U U^T\}}, \tag{18}$$

where $\text{Trace}\{\ \}$ is the sum of the diagonal elements of a matrix, O and U are orthonormal bases for the CSS matrix C and CMF matrix A, respectively, and ν is a MOG that describes the proximity between the fundamental subspaces of C and A. The value range of ν is zero to one, where a value closer to one indicates higher proximity, implying better color performance. Owing to its data-independent property, this method provided a major advantage in terms of optimization speed.

The figure of merit (FOM) proposed by Sharma and Trussell [10] was the second error metric selected. This metric uses the Jacobian matrix $J_f(t)$ to produce a linear approximation of the transformation of XYZ-LAB space to calculate the MSE in uniform color space:

$$\Delta E_{ab}{}^2 \cong E\{||J_F(t)(t - \hat{t})||_2^2\}. \tag{19}$$

The advantage of using this linearized error metric is that closed-form expressions can be obtained for both the optimal transformation and scanner error metric [10]. Here, we selected the simplified approximate perceptual FOM as the merit function:

$$q_{FOM} = \frac{\text{Trace}\{F_{Lab}^T F_{Lab} A_L^T K_r G (G^T K_r G + K_\eta)^{-1} G^T K_r A_L\}}{\text{Trace}\{F_{Lab}^T F_{Lab} A_L^T K_r A_L\}}, \tag{20}$$

where $K_r = E\{rr^T\}$ is the correlation matrix for the ensemble of the reflectance spectra of the sample, and K_η is the covariance matrix of the noise. In this study, we ignored the influence of noise, meaning that $K_\eta = 0$. F_{Lab} was replaced by the linear transformation F_{Lab} by calculating the Jacobian matrix at the white point. Like the MOG, the FOM takes a value in the range of zero to one, wherein a value closer to one indicates better color performance.

Finally, we used the ΔE_{ab}^* calculated by RPCC in Eq. (11) as the merit function to further optimize the filters. Compared with the results from MOG and FOM, the optimization results obtained using ΔE_{ab}^* could directly reflect the true color performance of the camera better.

To ensure the physical feasibility of the film and improve the optimization speed, we set the following constraints during the optimization process.

1. First, we constrained the range of values of the S_{BRC}, S_{RRC}, and S_{IR} filters synthesized using Gaussian functions, limiting the transmittance to always be between zero and one and making the maximum value approximately one.

2. For the BRC and RRC, to suppress the reflection of light back and forth within the X-cube prism, we needed to ensure that the two films could not have high reflectivity values within the same wavelength band, i.e., $(1 - S_{RRC}) \times (1 - S_{BRC}) < 0.02$.

3. The peak wavelengths of the three RGB channels had approximate optimal values of 450, 540, and 600 nm, respectively, with full width at half maximum values of 40 nm for B and 50–60 nm for R and G [11]. Correspondingly, we set the value ranges for the three sets of Gaussian parameters to speed up the optimization process.

4. Although the transmittance curve obtained by combining multiple Gaussian functions ensured the smoothness of the curve, it may still cause multiple peaks in the combined RGB spectrum during the optimization process. To simplify the design results and make them easier to process, we needed to also constrain the unimodality of the curve.

5. Finally, to allow the results after the film design to have a smaller spectrum shift, from a film design perspective, we needed to ensure that the transmittance curves of the BRC and RRC had greater steepness, which was helpful in reducing the spectral shifts caused by changes in the angle of incidence.

B. Optimization with the Consideration of Incident Angle

Optimization without consideration of incident angle could obtain a set of transmittance curves of RRC, BRC, and IR filters

calculated from Gaussian parameters. Using these curves as the target for thin film design, the initial film parameters could be obtained to calculate the CSS matrix $C(x, y)$ with the incident angle consideration according to Eqs. (14)–(16).

When constructing the merit function considering the incident angle, we first needed to select the FOV points on the image plane for use in the optimization process. Choosing more sampling points during optimization could undoubtedly help us comprehensively analyze the color performance of each position on the image plane, but it would further increase the calculation amount of the merit function, producing a significant impact on the subsequent film optimization speed. We took $(2n + 1) \times (2n + 1)$ sampling points uniformly on the image plane. The coordinate of the center point was $(0,0)$, and the range from $-n$ to n is taken in both x and y directions. Since the X-cube prism displayed symmetry in the horizontal direction (x direction), only half of the area in the $+x$ direction of the image plane needed to be considered in the actual analysis. In this case, the imaging light in the edge FOV had the largest incident angle change compared to the central FOV; the edge point was the point where the RGB response deviated the most from the central point. Additionally, the camera RGB response changed continuously on the image plane, so it was necessary only to optimize the color shift of the edge field point within an acceptable range; accordingly, the non-uniform color error caused by the incident angle could be corrected. According to the symmetry of the X-cube prism, we selected the central field point $(0,0)$ and two edge field points (n, n) and $(n, -n)$ in the $+x$ direction to calculate the merit function.

Here, we no longer used Gaussian parameters as inputs but directly optimized the thin film in the *Essential Macleod*. We used the incident angle distribution function $P(x, y, \theta)$ of the three sampling points as constant and calculated $F(\theta)$ from the current thin film as input; the CSS matrix $C(x, y)$ of the three sampling points can be calculated in each optimization iteration, and the corresponding $\Delta E_{ab}^*(x, y)$ can be calculated using Eq. (11). Additionally, we also needed to consider the color error value between the three sampling points because for the imaging system, we required all the points not only to have a low color error but also no obvious color errors between the areas on the image plane. The final merit function with the incident angle consideration can be written as

$$\varepsilon = \Delta E_0 + \Delta E_1 + \Delta E_2 + k(\Delta E_{01} + \Delta E_{02} + \Delta E_{12}),$$
(21)

where $\Delta E_0 = \Delta E_{ab}^*(0, 0)$, $\Delta E_1 = \Delta E_{ab}^*(n, n)$, and $\Delta E_2 = \Delta E_{ab}^*(n, -n)$ represent the color errors between the sampling point and real color. ΔE_{01}, ΔE_{02}, and ΔE_{12} are the ΔE_{ab}^* errors between the three sampling points, and k is the weight coefficient.

We wrote the merit function to the *Essential Macleod* software and used the thin film obtained by optimization without consideration of the incident angle as the starting point to carry out the optimization wherein the incident angle was considered. However, in *Essential Macleod*, if a custom merit function is used, each optimization can be run for only one film; therefore, we used the loop optimization method to optimize the three films. In this optimization loop, because we were directly optimizing the thin film, the constraints of limiting the

transmittance function to ensure film processability no longer applied; therefore, we removed constraints 3–5—mentioned in Section 3.A—and retained only constraints 1 and 2.

C. Non-Uniform Color Correction Based on Ray Tracing

After completing the film design while considering the incident angle, we could evaluate the color performance of the center and edge points using the parameters in the merit function. However, the parameters of the three sampling points alone could not intuitively show the color non-uniformity of the camera in the full FOV. We introduced the optimized film into the model of the optical system and used ray tracing in *LightTools* to directly count the CSS matrix $C(x, y)$ for all the $(n + 1)(2n + 1)$ sampling points in the $+x$ direction on the image plane. The CSS of all the positions on the image plane and their corresponding correction matrices could be obtained using the interpolation method, and independent color correction could be performed, thereby eliminating the influence of spectral shift on color uniformity. Finally, we used hyperspectral images to conduct imaging simulation experiments, which could simulate the color shift phenomenon in the X-cube prism. Using the simulated images, we could intuitively compare the color errors before and after optimization and correction.

4. EXPERIMENTS AND RESULTS

A. Results of Optimization without Consideration of Incident Angle

In the optimization without consideration of incident angle, we used 1269 Munsell color chips, 24-color Macbeth ColorChecker patches, and 57 additional surfaces [21] to comprise the reflectance sample r and CIE D65 as the light source L. The CIE 1931 2° Standard Observer was used as the CMFs matrix A. S_{RRC}, S_{BRC}, and S_{IR} were synthesized by trimmed Gaussian functions and combined with the lens transmission and the detector's response to obtain the camera's three-channel spectral sensitivity function C. Through Eqs. (1)–(11), we could calculate the CIELAB space color error ΔE_{ab}^* of the sample after RPCC from the camera response C, which could optimize the ideal film curve. When performing RPCC, we took the third degree root polynomial, that is, $i = 13$; and to achieve higher calculation accuracy, we used 1 nm interval sampling in the 380–780 nm range.

Since our initial structure was constructed via Gaussian function fitting with reference to the CMFs and the properties of the X-cube prism, the $\Delta E*_{ab}$ values of this initial point after RPCC reached 0.7692, where 2.3 ΔE_{ab}^* units corresponded to a just noticeable difference (JND) [22]. This initial structure, which did not consider the constraints, exhibited a relatively good color performance.

During optimization, we used MOG, FOM, and ΔE_{ab}^* as merit functions to optimize the transmittance curve of the film. The results of the three merit functions are shown in Table 1; the closer the values of MOG and FOM are to one, and the lower the ΔE_{ab}^* values are, the better the performance.

Table 1. Results of Optimizations without Consideration of Incident Angle

Designed Set	MOG	FOM	ΔE_{ab}^*
Initial point	0.9493	0.9596	0.7692
Gauss set 1, MOG	0.9717	0.9439	1.0542
Gauss set 2, FOM	0.9436	0.9854	0.3706
Gauss set 3, RPCC	0.9451	0.9848	0.3469

With its sample-independent and fast calculation speed, the MOG could quickly obtain the preliminary Gauss set 1 from the initial structure under the condition that the constraints were satisfied. As shown in Table 1, the MOG of Gauss set 1 has increased from 0.9493 for the initial structure to 0.9717, but the ΔE_{ab}^* here is worse than that of the initial structure. This was because part of the color performance was sacrificed to preferentially satisfy the constraints during optimization, but it also demonstrated that the MOG had no strong correlation with the ΔE_{ab}^* of uniform color space.

Subsequently, we used the results of MOG optimization as the input and then used the FOM as the merit function for the second optimization. Here, we ignored system noise and selected the approximate perceptual FOM equation for a uniform color space as the merit function. Compared with Gauss set 1 for MOG optimization, the FOM value and ΔE_{ab}^* of Gauss set 2 improved significantly.

Finally, we used the results from FOM optimization as the input and then used ΔE_{ab}^* calculated from RPCC to perform the final optimization. Gauss set 3 achieved the lowest ΔE_{ab}^* error. It could be found from the results that the FOM has a strong correlation with the ΔE_{ab}^* of uniform color space, and FOM has the advantage of faster optimization speed with its linearized calculation. However, due to the introduction of the RPCC method, directly using the ΔE_{ab}^* calculated by the RPCC to revise the optimization results of the FOM could further improve the color performance of the filter set.

From the transmittance curves for each result, as shown in Fig. 3, we inferred that owing to the stricter optimization constraints, the transmittance curves starting from Gauss set 1

for MOG optimization had been finalized, and Gauss set 3 showed very few curve changes when compared with the FOM optimization results.

B. Thin Film Design Results

We took Gauss set 3 to be the ideal transmittance curve to design the film, and filter set 1 for the final design results, as shown in Fig. 4(a). The IR-cut film had an angle of incidence of $0 \pm 10°$, and its transmittance curve did not deviate significantly when the angle of incidence was small. The designed result for the IR-cut film was consistent with the ideal value. When designing the BRC and RRC films, we ensured the fitting degree of the transmittance curve at an angle of incidence of 45°. Simultaneously, the spectral shift at 50% transmittance when the chief ray of the edge field was incident at 41° and 49° was added to the optimization target.

The results showed that when the angle changed, the overall trend of the BRC transmittance curve remained the same, but the deviation was large. When the angle of incidence was $45° \pm 4°$, the 50% transmittance position was shifted by 21 nm. For RRC, because the operating band was different from that of BRC, the 50% transmittance position shift reached 83 nm when the angle of incidence was $45° \pm 4°$ in the first edition. If the shift in the spectrum was too large, it may have caused a color error that would be difficult to correct. Therefore, in the subsequent thin film optimization, we relaxed the fit of the curve in relative terms to obtain a smaller spectral shift. The optimized results for the final edition of filter set 1 reduced the 50% transmittance position shift to 48 nm for the RRC. However, the overall curve trend shows a deviation from the ideal value, as illustrated in the figure.

C. Results of Optimization with Incident Angle Consideration

After obtaining the initial thin film, we used the method discussed in Section 3.B to carry out the optimization while
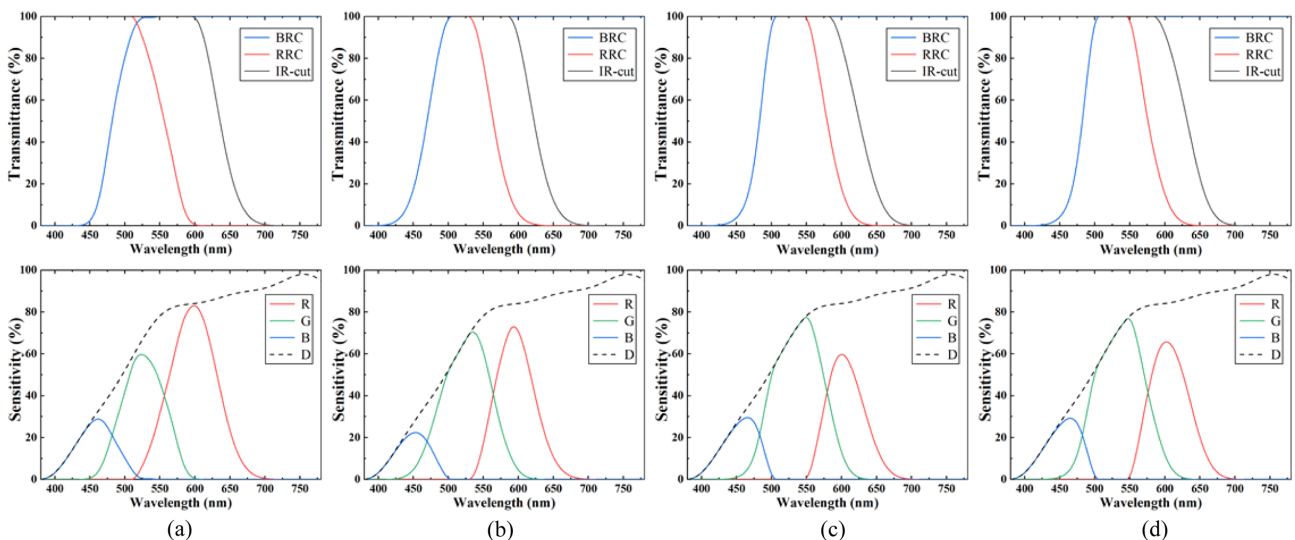

Fig. 3. Filter sets and corresponding CSS functions RGB and CCD response D (combined with lens transmittance) obtained with (a) initialization; (b) MOG; (c) FOM; (d) ΔE_{ab}^*.
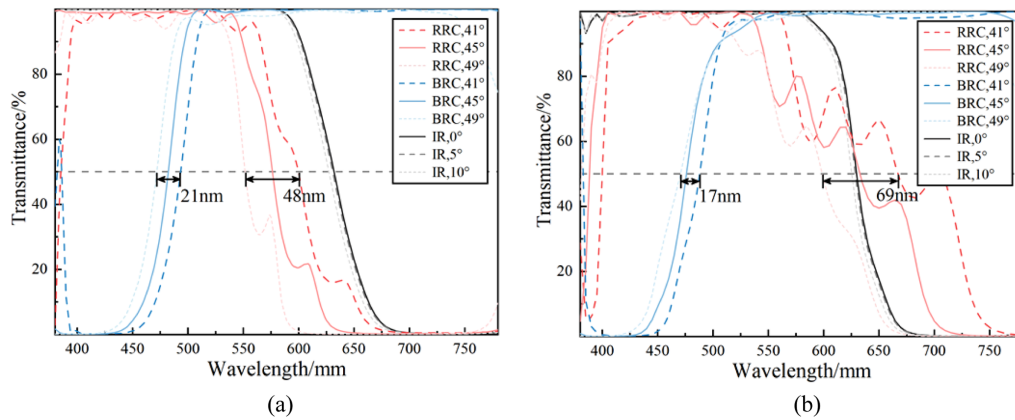
Fig. 4. Spectra of RRC, BRC, and IR-cut. (a) Filter set 1 and (b) filter set 2.

considering the incident angle. Since the thin film was optimized directly under this method, in each iteration, it was necessary to calculate the transmission characteristics $F(\theta)$ through the thin film, calculate the CSS matrix $C(x, y)$ in combination with the incident angle distribution $P(x, y, \theta)$ at the three sampling points, and finally calculate the color error $\Delta E_{ab}^*(x, y)$ of all samples using the RPCC method. The computational complexity of this process was much higher than that of the optimization of Gauss parameters. To speed up the optimization process, we used only the reflectance of the 24-color Macbeth ColorChecker as the sample and increased the spectral sampling interval to 5 nm. When calculating $P(x, y, \theta)$ and $F(\theta)$, the incident angle θ on the film was in the range of $34°$–$56°$ and had a sampling interval of $1°$.

The transmittance of filter set 2 through the optimization loop of the three films of the RRC, BRC, and IR-cut is shown in Fig. 4(b). From the transmittance curve, because some of the constraints on the transmittance were canceled in the optimization process, the curve of the film was obviously different from the ideal value obtained by optimization without consideration of incident angle. In the incident angle range of $45° \pm 4°$, the spectral shift of the BRC decreased from 21 to 17 nm, while the shift of the RRC expanded from 48 to 69 nm.

However, when we combined the incident angle distribution $P(x, y, \theta)$ to analyze the spectral characteristics of the broad beam, as shown in Fig. 5, the CSS of filter sets 1 and 2 are not

significantly different in terms of the curve shape and peak wavelength. After optimization while considering the incident angle, the difference between the spectral peak positions of the three sampling points was significantly smaller, and without the steepness constraint, there was a larger repeated area among the three bands of R, G, and B, making it closer to the characteristics of the CMFs.

We analyzed the average color error of the sampling points and the error between them for the two filter sets. The results are shown in Table 2, where each color error is the mean ΔE_{ab}^* value of the 24-color Macbeth ColorChecker after RPCC.

Since we performed independent RPCC for all three sample points, the mean and max ΔE_{ab}^* for both filter sets were less than 2.3 units of the JND, and the two filter sets achieved relatively good color performance. Furthermore, because the color errors between the center and edge points represented the maximum color deviation on the image plane, the results proved that the independent correction method could effectively suppress the color deviation of the entire FOV. After optimization while considering the incident angle, the color error of the three sampling points in filter set 1 was slightly reduced compared with that of filter set 1, and the color error between the three sampling points was significantly reduced. These results showed that optimization while considering the incident angle could reduce the color non-uniformity between the points on the image plane while preserving the overall color performance.
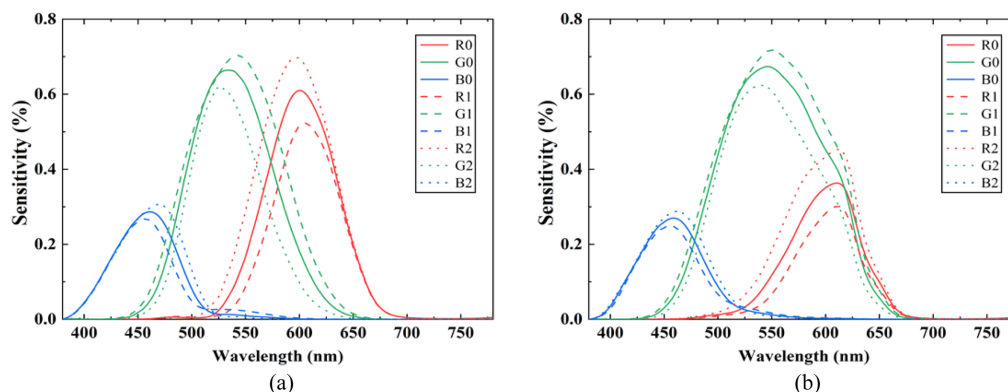

Fig. 5. CSS for (a) filter set 1 and (b) filter set 2.

Table 2.   **Color Error of Two Filter Sets**

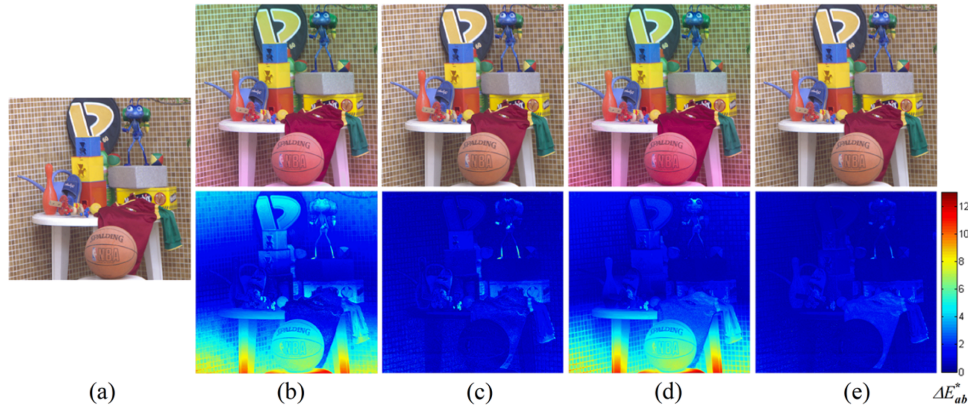|		Color Error with Real Color			Color Error between Points		
		ΔE_0	ΔE_1	ΔE_2	ΔE_{01}	ΔE_{02}	ΔE_{12}
Filter set 1	Mean	0.3918	0.4373	0.4864	0.2988	0.2913	0.5817
	Max	0.8869	0.9030	1.5853	0.8463	0.9521	1.6654
Filter set 2	Mean	0.3813	0.3578	0.4422	0.1414	0.1556	0.2920
	Max	0.8586	0.8946	1.1807	0.4943	0.4871	0.9798

Fig. 6.   Hyperspectral simulated image and color error distribution for two filter sets. (a) Original image. Filter set 1 (b) before and (c) after independent correction. Filter set 2 before (d) and (e) after independent correction.

D. Results of Independent Color Correction

To visually display the color non-uniformity distribution in the image, we took $n = 8$ and 9×17 sampling points in the $+x$ direction of the image plane and then calculated the CSS matrix $C(x, y)$ of these sampling points in *LightTools*. Since the calculated $C(x, y)$ was obtained by tracing many imaging rays and counting the power of rays in 81 intervals per 5 nm interval, the data we obtained were a $9 \times 17 \times 81 \times 3$ matrix. We performed smooth fitting processing on the obtained data on the image plane, took sampling points, and then interpolated in the spectral direction to obtain spectral data at 1 nm intervals. Finally, by mirroring the x direction, a $160 \times 160 \times 401 \times 3$ matrix $C(x, y)$ could be obtained for the imaging simulation experiments. We used the hyperspectral image [23] to perform the simulation under the two filter sets and calculated the simulated image and color distribution before and after independent correction. The results are shown in Fig. 6.

Figures 6(b) and 6(d), which show tsimulated images, indicate that the color non-uniformity on the image plane mainly occurs in the y-axis direction, and the maximum color deviation occurs at the edge of the image plane as we expected. In Figs. 6(c) and 6(e), the color non-uniformity of the two filter sets has been significantly reduced after independent color correction for the entire FOV. The mean value of ΔE_{ab}^* for filter set 1 after correction was 0.8408, and the maximum value was 13.1530. The mean value of ΔE_{ab}^* for filter set 2 after correction was 0.7184, and the maximum value was 8.5956, and its performance was much better than that when the incident angle was not considered. The hyperspectral image simulation verified the effectiveness and necessity of independent color correction for the X-cube prism 3CCD camera, and the comparison of color error values for two filter sets also showed that the optimization

while considering the incident angle could further improve the color performance of the camera.

5. CONCLUSION

In this study, a filter design and color correction methods were proposed to improve the color performance of an X-cube prism 3CCD camera. Based on the optical properties of optical thin film and X-prism, the effect of the spectral shift caused by the incident angle on the camera's color performance was considered during the filter optimization and color correction process. We inferred from the hyperspectral image simulation results that the independent correction method could significantly reduce the color non-uniformity, verifying the effectiveness and necessity of independent color correction for the X-cube prism 3CCD camera. Comparing the simulation results of the two filter sets, we also inferred that the proposed optimization method could further improve the color performance of the camera.

This study provided a basis for solving the color deviation problem of X-prism 3CCD cameras. However, due to the limitation of the design software and the excessive calculation, the optimization speed of the proposed method was slow, which was not conducive to the adjustment of constraints and merit function during optimization. At the same time, all the optical models in this study were based on the fixed optical lens in front of the X-cube prism, which meant that any change in the front lens group might bring about different ray tracing results. Therefore, an optimization method with a faster calculation speed and a correction method with broader applicability will be the focus of future research.

Disclosures.   The authors declare no conflicts of interest.

Data availability. Data underlying the results presented in this paper are available in Refs. [21,23].

REFERENCES

1. N. Ohta and A. R. Robertson, *Colorimetry: Fundamentals and Applications*, Wiley-IS&T series in imaging science and technology (Wiley, 2005).
2. W. D. Wright, "A re-determination of the trichromatic coefficients of the spectral colours," Trans. Opt. Soc. **30**, 141–164 (1929).
3. J. Guild, "The colorimetric properties of the spectrum," Philos. Trans. R. Soc. Lond. Ser. Contain, Pap. Math. Phys. Character **230**, 149–187 (1931).
4. R. Luther, "Aus dem Gebiet der Farbreizmetrik, Nr.," Z. Tech. Physik **8**, 540–558 (1927).
5. H. E. J. Neugebauer, "Quality factor for filters whose spectral transmittances are different from color mixture curves, and its application to color photography," J. Opt. Soc. Am. **46**, 821–824 (1956).
6. P. L. Vora and H. J. Trussell, "Measure of goodness of a set of color-scanning filters," J. Opt. Soc. Am. A **10**, 1499–1508 (1993).
7. P. L. Vora and H. J. Trussell, "Mathematical methods for the design of color scanning filters," IEEE Trans. Image Process. **6**, 312–320 (1997).
8. M. J. Vrhel and H. J. Trussell, "Filter considerations in color correction," IEEE Trans. Image Process. **3**, 147–161 (1994).
9. M. Wolski, C. A. Bouman, J. P. Allebach, and E. Walowit, "Optimization of sensor response functions for colorimetry of reflective and emissive objects," IEEE Trans. Image Process. **5**, 507–517 (1996).
10. G. Sharma and H. J. Trussell, "Figures of merit for color scanners," IEEE Trans. Image Process. **6**, 990–1001 (1997).
11. S. Quan, N. Ohta, R. S. Berns, X. Jiang, and N. Katoh, *Unified Measure of Goodness and Optimal Design of Spectral Sensitivity Functions* (2002), Vol. **14**.
12. G. D. Finlayson, M. Mackiewicz, and A. Hurlbert, "Color correction using root-polynomial regression," IEEE Trans. Image Process. **24**, 1460–1470 (2015).
13. H. Kang, "Colour scanner calibration," J. Imaging Sci. Technol. **36**, 162–170 (1992).
14. G. Hong, M. R. Luo, and P. A. Rhodes, "A study of digital camera colorimetric characterization based on polynomial modeling," Color Res. Appl. **26**, 76–84 (2001).
15. P.-C. Hung, "Colorimetric calibration in electronic imaging devices using a look-up-table model and interpolations," J. Electron. Imaging **2**, 53 (1993).
16. M. Mackiewicz, C. F. Andersen, and G. Finlayson, "Method for hue plane preserving color correction," J. Opt. Soc. Am. A **33**, 2166–2177 (2016).
17. P. G. Anderson, "Neural network applications to the color scanner and printer calibrations," J. Electron. Imaging **1**, 125 (1992).
18. H. S. Kwok, P. W. Cheng, H. C. Huang, H. F. Li, Z. R. Zheng, P. F. Gu, and X. Liu, "Trichroic prism assembly for separating and recombining colors in a compact projection display," Appl. Opt. **39**, 168–172 (2000).
19. G. Wyszecki and W. S. Stiles, *Color Science: Concepts and Methods, Quantitative Data, and Formulae*, Wiley Classics Library (Wiley, 2000).
20. G. H. Golub and C. F. Van Loan, *Matrix Computations*, 4th ed., Johns hopkins studies in the mathematical sciences (The Johns Hopkins University, 2013).
21. K. Barnard, L. Martin, B. Funt, and A. Coath, "A data set for color research," Color Res. Appl. **27**, 147–151 (2002).
22. G. Sharma and H. J. Trussell, "Digital color imaging," IEEE Trans. Image Process. **6**, 901–932 (1997).
23. S. M. C. Nascimento, F. P. Ferreira, and D. H. Foster, "Statistics of spatial cone-excitation ratios in natural scenes," J. Opt. Soc. Am. A **19**, 1484–1490 (2002).